JGR Earth Surface

RESEARCH ARTICLE
10.1029/2019JF005452

Ooid Cortical Stratigraphy Reveals Common Histories of Individual Co-occurring Sedimentary Grains

Elizabeth J. Trower[1], Sophia L. Bridgers[2], Michael P. Lamb[3], and Woodward W. Fischer[3]

[1]Department of Geological Sciences, University of Colorado Boulder, Boulder, CO, USA, [2]Department of Atmospheric and Ocean Sciences, University of Colorado Boulder, Boulder, CO, USA, [3]Division of Geological and Planetary Sciences, California Institute of Technology, Pasadena, CA, USA

Key Points:
- Surface-normal precipitation and collisional abrasion produce different trajectories in ooid shape
- Cortical layer boundaries in an individual ooid can be inverted to reconstruct that grain's history of growth and abrasion
- Ooids found together from different locations across Great Salt Lake, UT, share common sets of growth-abrasion histories

Supporting Information:
- Supporting Information S1

Correspondence to:
E. J. Trower,
lizzy.trower@colorado.edu

Citation:
Trower, E. J., Bridgers, S. L., Lamb, M. P., & Fischer, W. W. (2020). Ooid cortical stratigraphy reveals common histories of individual co-occurring sedimentary grains. *Journal of Geophysical Research: Earth Surface*, *125*, e2019JF005452. https://doi.org/10.1029/2019JF005452

Received 26 NOV 2019
Accepted 26 MAY 2020

Abstract Ooids are a common type of carbonate sand grain that form through a combination of constructive and destructive mechanisms: growth via precipitation and diminution via physical abrasion. Because growth and abrasion obey distinct morphometric rules, we developed an approach to quantitatively constrain the history of growth and abrasion of individual ooid grains using the record of evolving particle shape preserved by their cortical layers. We designed a model to simulate $>10^6$ possible growth-abrasion histories for each pair of cortical layer bounding surfaces in an individual ooid. Estimates for the durations of growth and abrasion of each cortical layer were obtained by identifying the simulated history that best fit the observed particle shape. We applied this approach to thin sections of "modern" lacustrine ooids collected from several locations in the Great Salt Lake (GSL), UT, to assess the spatial and temporal variability of environmental conditions from the perspective of individual grains within a single deposit. We found that GSL ooids do not all share the same histories: Clustering ooid histories by a Fréchet distance metric revealed commonalities between grains found together locally within a deposit but distinct differences between subpopulations shared among localities across the GSL. These results support the tacit view that carbonate sedimentary grains found together in the environment do reflect a common history of sediment transport. This general approach to invert ooid cortical stratigraphy can be applied to characterize environmental variability over <1,000 year timescales in both marine and lacustrine ooid grainstones of any geologic age.

Plain Language Summary Ooids are sand grains that are composed of a series of concentric layers of calcium carbonate precipitated around a smaller particle. We hypothesized that the layers in an ooid preserve a record of the episodes of growth and abrasion experienced by that grain because these processes change the shape of the grain in distinct and unique ways. We designed a model to simulate many possible shapes for each layer resulting from different combinations of growth and abrasion and identified each ooid's history by finding the combination that best fit the actual layers in the ooid. We applied this model to ooids we collected from three locations in Great Salt Lake (UT) and found several distinct sets of histories shared by grains from all the locations. These data support an implicit assumption made by sedimentologists—that calcium carbonate sand grains deposited together share similar transport histories. Our approach can be applied to ancient ooids to assess the variability of paleoenvironments over shorter timescales than existing techniques.

1. Introduction

Ooids are a type of carbonate sand grain composed of a concentrically layered cortex precipitated around a central nucleus that occur commonly in carbonate successions of all ages from both marine and lacustrine settings. They are unique among sedimentary grains in that they form through both constructive and destructive mechanisms: growth via surface-normal precipitation and diminution via physical abrasion (Bathurst, 1975; Heller et al., 1980; Trower et al., 2017). Each ooid cortex keeps a record of this process in the form of its sequence of concentric layers—a kind of stratigraphy on the scale of cortical layers inside a single accreting grain. As with typical sedimentary successions, Steno's (1669) stratigraphic relationships also apply to the cortical stratigraphy contained within laminae of ooids, albeit on a smaller spatial scale (Figure 1): (1) superposition—younger cortical layers occur further away radially from the nucleus than do older cortical layers; (2) original horizontality—cortical layers precipitate normal to the antecedent grain surface; and (3) crosscutting relationships—where truncation relationships and surfaces reflect the relative timing over which those layers or surfaces were emplaced. Furthermore, ooid cortices are subject to the same

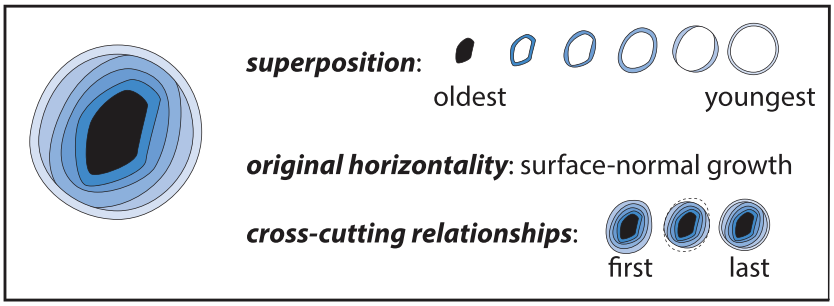

Figure 1. Schematic illustration of logical stratigraphic constraints as applied to ooid cortices in cross section. Superposition requires that exterior cortical layers are younger than interior cortical layers, where decreasing age is illustrated by lighter shades of blue. Original horizontality requires that growth occurs in a surface-normal direction. Crosscutting relationships requires that crosscutting surfaces are younger than the layers they truncate: In this case, this is represented by an abrasion surface underlying the outermost cortical layer, which truncates the two adjacent interior cortical layers.

types of processes that are recorded in any stratigraphic record: deposition—in the case of an ooid, surface-normal precipitation; erosion—in the case of an ooid, abrasion during transport or bioerosion by endolithic microorganisms; and hiatuses in deposition. Therefore, we followed the logic of Sandberg (1975) in that each cortical layer represents a "deposit," that is, an interval of net precipitation on the ooid surface, and each contact between layers reflects an unconformity, that is, an interval of net abrasion juxtaposed between growth episodes.

Previous authors recognized that the stratigraphic information recorded in ooid cortices could potentially be used to discern paleoenvironmental conditions, specifically in the case of bimineralic ooids whose cortices contained layers composed of two different $CaCO_3$ polymorphs—calcite and aragonite. In bimineralic ooids, cortices are thought to reflect varying primary fluid chemistry (Algeo & Watson, 1995; Chow & James, 1987; Tucker, 1984). However, applications of the concept of ooid cortical stratigraphy have remained limited to qualitative assessments (Sandberg, 1975), in large part because there has not been a framework with which to quantify and compare these stratigraphic relationships within ooid cortices. This type of stratigraphic information could be useful to answer enduring questions about ooid genesis, variability of key paleoenvironmental parameters over short timescales, and the transport histories of sedimentary particles. For example, does ooid nucleation occur at a single point in time, or are new ooids continuously nucleating in a system that may contain active older ooids? Do ooids record changes in carbonate saturation state or current energy that are subtler than those reflected in bimineralic ooids—environmental variations, in other words, that might be below the temporal resolution of typical stratigraphic records? More broadly, it is common in sedimentology to presume that carbonate sedimentary grains of similar sizes deposited together have shared sediment transport histories; ooid cortical stratigraphy could be used to begin to quantitatively test this assumption.

We developed an approach to study ooid cortical stratigraphy using grain shape, for example, roundness, sphericity, and aspect ratio, to quantitatively constrain an individual grain's history of growth and abrasion. Recent modeling work predicted that surface-normal growth, collisional abrasion, and frictional abrasion each produce distinguishable trajectories in particle shape (Sipos et al., 2018). Because each cortical layer provides a record of the former grain shape and size, the radial differences between adjacent bounding surfaces can be used to estimate the volumes of carbonate added via growth and subsequently removed via abrasion during the deposition of each layer. These data then can be inverted to constrain the length of time associated with each cortical layer using recent experimental constraints on ooid growth and abrasion rates, which are both functions of grain size (Trower et al., 2017). We applied this approach to thin sections of modern lacustrine ooids from several locations in the Great Salt Lake (GSL), UT, to demonstrate how cortical stratigraphy via ooid shape can be used to assess the spatial and temporal variability of environmental conditions—from the perspective of individual grains within a single deposit.

2. Model Development and Implementation

2.1. Model Rationale

Describing a particle's surface requires three dimensions [(x, y, z) or (r, θ, φ)], but in order to use the data widely available from typical geological thin section preparations, we employed a two-dimensional

spherical segment treatment of particle shape change. For particles with aspect ratios less than 3:1, the maximum deviation between 2-D and 3-D models of shape change due to abrasion is <10% (Sipos et al., 2018), and so that constraint gives a sense of the potential uncertainty introduced by this simplification. The following approach therefore assumed an ooid viewed in a cross-sectional plane that includes the maximum diameter (i.e., major axis) and the center of mass.

Grain shape has long been applied as a qualitative metric for the extent of transport of siliciclastic sediment: Angular grains have experienced less transport distance than have rounded grains, whose apices have been smoothed by abrasion. Recent studies have used experiments, modeling, and field observations to quantitatively describe the process of rounding of sedimentary particles (Domokos et al., 2014; Miller et al., 2014; Novák-Szabó et al., 2018). These studies confirmed Bloore's (1977) prediction that particle rounding follows a predictable trajectory as a function of the particle's evolving shape in 2-D:

$$v_{\text{abrasion}} = 1 + c_1\kappa, \tag{1}$$

where v_{abrasion} is the dimensionless inward-normal rate of diminution for a point on the particle surface, c_1 is the average perimeter of abrading particles (units of length), and κ is the local curvature of the particle surface at that point (units of inverse length). The $c_1\kappa$ term describes abrasion resulting from collisions when particles are saltating. Sipos et al. (2018) built on this model by introducing a term that described abrasion resulting from friction when particles are rolling or sliding: $c_2\delta\cos(\gamma)$, where c_2 is a constant scaling the contribution of frictional abrasion relative to collisional abrasion, δ is the distance between that point and the longest diameter, and γ is the angle between a tangent line at that point and the longest diameter. Given an initial particle shape and a transport mode, one can therefore predict the trajectory of that shape over a series of dimensionless time steps. This prediction can be scaled, that is, placed in the context of specific length and time units, using the experimental data and ooid abrasion rate model developed by Trower et al. (2017), which enables one to determine a grain-averaged radial abrasion rate ($R_{\text{abrasion, grain avg}}$) for particle-bed impacts as a function of grain size and transport mode:

$$R_{\text{abrasion,grain avg}} = \frac{A_1\rho_s Y w_i^3 D}{6k_v\sigma_T^2 H_{\text{fall}}}, \tag{2}$$

where $A_1 = 0.36$ is a dimensionless coefficient; ρ_s is sediment density (2.8 g/cm^3 for aragonite); w_i is impact velocity normal to the bed calculated following Lamb et al. (2008); D is the particle diameter; H_{fall} is the typical distance above the bed that a particle is transported; and σ_T (tensile strength), Y (Young's modulus), and k_v (a dimensionless coefficient that accounts for differences in material properties between the particles and the bed surface) were set following Trower et al. (2017).

Abrasion rates calculated using the Trower et al. (2017) model can be used to scale v_{abrasion} for each point along the surface, defined in polar coordinates (r, θ), such that while the localization of abrasion is sensitive to the grain's surface geometry, their average is equal to the grain-averaged radial abrasion rate:

$$R_{\text{abrasion}}(r,\theta) = v_{\text{abrasion}}(r,\theta)\cdot 2\pi R_{\text{abrasion,grain avg}}\cdot\left(\int_0^{2\pi} v_{\text{abrasion}}(r,\theta)d\theta\right)^{-1}. \tag{3}$$

Ooids typically occur in environments where they are transported near the threshold of suspension (Trower et al., 2018), and grain-averaged abrasion rates are minimized near the threshold of motion (where frictional abrasion from sliding would be important), and thus, we assumed that collisional abrasion dominates frictional abrasion and used $c_2 = 0$ in the following analysis (Novák-Szabó et al., 2018). This assumption was evaluated using the results of the grain shape analysis.

Ooid growth is thought to occur via the precipitation of a surface-normal layer of equal thickness for each point on the grain surface (Bathurst, 1975; Davies et al., 1978; Ferguson et al., 1978; Heller et al., 1980; Simone, 1980; Sumner & Grotzinger, 1993). This process impacts grain shape in a predictable manner, analogous to the surface-normal growth term in the Kardar-Parisi-Zhang equation (Kardar et al., 1986; Maritan et al., 1992; Marsili et al., 1996; Sipos et al., 2018):

$$v_{\text{growth}}(r,\theta) = p, \tag{4}$$

where v_{growth} is the dimensionless outward-normal rate of growth for a point on the particle surface and p is a constant for all (r, θ). This equation also can be scaled using a carbonate precipitation rate based on the chemistry (e.g., saturation state) of the fluid, such as the empirical rate equation determined by Zhong and Mucci (1989):

$$R_{\text{growth}} = 10^6 \cdot k\left(\Omega_{\text{aragonite}} - 1\right)^n \cdot \frac{M(\text{CaCO3})}{\rho_{\text{CaCO3}}}, \tag{5}$$

$$v_{\text{growth}}(r,\theta) = R_{\text{growth}}, \tag{6}$$

where R_{growth} is the outward-normal growth rate for a point on the surface in units of μm/hr, k is the rate constant in units of μmol/m^2/hr, $\Omega_{\text{aragonite}}$ is the saturation state of aragonite, n is the reaction order, M ($CaCO_3$) is the molar mass of calcium carbonate in units of g/mol, and ρ_{CaCO3} is the density of aragonite (2.8 g/cm^3). For cases in which ooids are composed of calcite or other minerals, Ω, k, and n can be modified based on the thermodynamic and kinetic properties specific to the precipitation of any phase. Equation 5 incorporates an assumption that ooid growth rate is a function of chemical properties of the system—that is, that rate is primarily controlled by abiotic parameters. However, Equation 4 could be scaled using different rate relationships based on microbially mediated precipitation mechanisms if such rate equations are developed in the future.

Abrasion and surface-normal growth relationships predict distinct morphometric trajectories in particle shape, specifically that abrasion is more efficient at rounding and reducing elongation (Figure 2). Sipos et al. (2018) and Sipos (2020) used the rationale outlined above to hypothesize that "mature" ooid shapes should approach one of a suite of "equilibrium" shapes. Yet the conditions under which ooids form, including carbonate saturation state and bed shear velocity, are expected to change over the lifetime of an ooid (Bathurst, 1975; Davies et al., 1978; Mariotti et al., 2018; Newell et al., 1960; Trower et al., 2017), so the equilibrium shape may be as dynamic as the equilibrium size. Nevertheless, the shapes of the bounding surfaces of individual cortical layers each represent snapshots of the grain's shape at different points in its history. To reconstruct histories of these grains, we studied the patterns of change in ooid shape by extracting the geometries present in successive cortical layers within individual ooids collected from the environment; our approach aimed to interpret the integrated records of growth and abrasion recorded by each of these snapshots. Figure 2 illustrates five example histories for the same nucleus: (a) an ooid subject to only growth and no abrasion; (b) an ooid that experiences several episodes of abrasion; (c) an ooid that experiences abrasion for twice as long as in case b; (d) an ooid with the same as case c, but partitioned into one less stage; and (e) an ooid with the same cumulative growth and abrasion intervals as cases c and d but with only a single episode. In each case, the shapes of time-equivalent bounding surfaces differ, reflecting distinct growth-abrasion histories.

2.2. Ooid Shape as an Inverse Problem

We hypothesized it might be possible to approach ooid shape with time as an inverse problem, using the shapes of successive ooid cortical layers to constrain and compare the sets of net-growth and net-abrasion steps experienced by many ooids within and among different populations. We developed an algorithm to identify cortical layer bounding surfaces from a thin section image of an ooid, simulate a large set of possible bounding surfaces resulting from many growth-abrasion histories, and identify the best fit growth-abrasion history. Notably, this model formulation did not account for the possibility of additional growth and abrasion steps that were not preserved in the ooid cortex (e.g., additional cortical layers and associated boundaries that were totally erased by a subsequent abrasion event; Sadler, 1994). We designed a test to assess how such cases might influence the model results (see section 2.3).

2.2.1. Ooid Image Selection and Analysis

We made the assumption that the spherical segments presented by an ooid in thin section (far thinner than the particle size) cut through the center of mass of the nucleus and that the cross section includes the major axis about which the grain is roughly radially symmetric. Since most natural ooid populations display some, albeit mild, variance in grain size (e.g., Trower et al., 2018), even sectioning through a monolayer of ooids

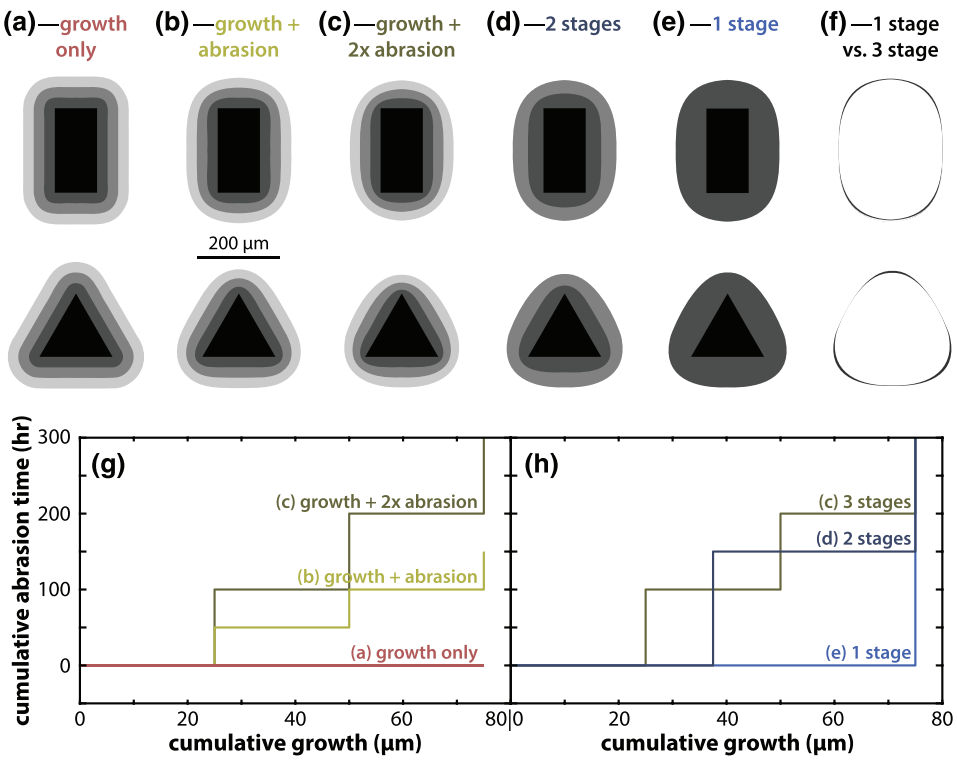

Figure 2. (a–f) Representative examples of how growth and abrasion affect ooid shape for (top row) elongated and (bottom row) angular nuclei and associated growth-abrasion history plots. (a) A nucleus (black) with three cortical layers (gray shades) precipitated via three growth episodes, with no abrasion. (b) The same increments of surface-normal growth as in (a) but punctuated by episodes of net abrasion between each growth episode. (c) The same increments of surface-normal growth as in (a) but punctuated by episodes of net abrasion between each growth episode, with double the abrasion duration in (b). (d) The same total growth increments and abrasion time as in (c) but incurred over only two growth-abrasion episodes rather than three. (e) Similar to (d), the same total growth increments and abrasion time as in (c) but incurred over only a single growth-abrasion episode. (f) The difference between the outermost surface in (e) versus (c), illustrating that partitioning the same overall total growth and abrasion into fewer episodes produces a slightly different shape. The equivalent difference between (d) and (c) is not shown because it is not legible at this scale. (g–h) Growth-abrasion history plots corresponding to the examples shown in (a)–(f) illustrated as step function plots. Growth increments are horizontal steps and abrasion increments are vertical steps: (g) identical amounts of growth but different abrasion durations, corresponding to the cortical layers in (a)–(c); (h) growth-abrasion histories with the same cumulative abrasion and cumulative growth but different numbers of growth-abrasion stages, corresponding to the cortical layers in (c)–(e).

embedded in epoxy would not result in ideal cross sections for all the grains—the centers of some nuclei would inevitably lie either above or below the plane of the thin section. Instead, we developed a set of selection criteria to identify suitable ooids in thin section, prepared either as loose sediment embedded in epoxy or from a lithified sample. These selection criteria included: (1) inclusion of the nucleus, indicating the cross-section cuts close to the center of the ooid; (2) occurrence of multiple cortical layers that could confidently be traced around the entire ooid (i.e., eliminating poorly preserved ooids in which cortical layer boundaries have been obscured by endolithic microboring, recrystallization, or some other fabric-destructive process); and (3) ooids with angular and/or elongated nuclei. The latter criterion was included because we predicted that the family of possible cortical layers resulting from surface-normal growth or collisional abrasion should be most distinct for these cases, in contrast with nuclei with circular cross sections. Selection of appropriate grains is a potential source of uncertainty, because it is likely that this selection method included at least some cases where the ooid cross section does not pass through the center of the grain and include the major axis. We implemented two approaches to address this issue: (1) characterizing the growth-abrasion history of many ooids from a sample, reducing the influence of any single grain on the outcome; and (2) developing an approach to evaluate misfit of the best fit history for each grain (see section 2.2.2), because cross sections that do not fulfill the model assumptions will not follow the morphometric rules defined in section 2.1. The bounding surfaces of the nucleus and cortical layers for each selected ooid were digitized and transformed into polar coordinates (r, θ) for 2,000 evenly spaced values of $\theta = (0, 2\pi]$; we chose only bounding surfaces that could confidently be traced around the

full perimeter of each ooid and assessed the sensitivity of the model to the number of cortical layers chosen (see below).

2.2.2. Simulating Growth-Abrasion Histories for an Individual Cortical Layer

Starting with the perimeter of the nucleus and the innermost cortical layer, growth-abrasion histories were simulated for each pair of adjacent bounding surfaces; the best fit trace for each surface was used as the initial condition for simulating the next layer. The minimum growth increment was set as the smallest amount of surface-normal growth required for the radius of the simulated growth trace to be greater than the radius of the goal layer trace for $\theta = (0, 2\pi]$. Additional growth increments were either applied as increments of set surface-normal thickness or parameterized as a function of Ω and time. Each possible growth surface was calculated by creating a circle with a radius equal to the defined growth increment around each (r, θ), identifying the coordinates of the minimum polyshape bounding this suite of circles, and transforming those coordinates to 2,000 evenly spaced values of $\theta = (0, 2\pi]$.

After simulating possible surfaces resulting from growth, we subjected each to a series of abrasion increments, such that the total number of possible surfaces resulting from some combination of growth and abrasion was the product of number of growth increments and number of abrasion increments. The grain-averaged abrasion rate, $R_{\text{abrasion, grain avg}}$, (in units of length/time) was calculated following Trower et al. (2017) for the first time step and after each subsequent 1,000 time steps. This interval was chosen to because the abrasion rate did not change significantly over 1,000 steps (for a grain with a 300 μm diameter, abrasion rate decreases by 0.014% over 1,000 time steps; Figure S1 in the supporting information). Following Equation 2, ooid abrasion rate is dependent on grain diameter, D, which was determined as the minimum diameter of the cortical layer trace for that time step; bed shear velocity, u_*; and water depth, H. Since typical ooids are approximately rotationally symmetric about their maximum diameter (i.e., major axis) (Heller et al., 1980; Sipos et al., 2018), the minor and intermediate axis dimensions of an ooid are approximately equal to one another and were thereby constrained by measuring the minimum diameter of an ooid in a cross section. Bed shear velocity was calculated using an assumed constant Rouse number, $P = \frac{w_s}{\mathrm{K}u_*}$, where $K = 0.41$ is the von Kárman constant and w_s is settling velocity calculated following Dietrich (1982) and assuming ooid density $\rho_s = 2.8$ g/cm^3 and fluid density ρ_f set according to the system considered (e.g., 1.02 g/cm^3 for seawater). For current-rippled ooids, bed shear velocity alternatively or additionally could be constrained using ripple wavelength and the dimensionless Yalin number, $\chi = Re_p\sqrt{\tau_*}$, where $Re_p = \frac{u_* D}{\nu}$ is the particle Reynolds number and $\tau_* = \frac{\rho_f u_*^2}{\left(\rho_s - \rho_f\right) g D}$ is Shields stress (Lapotre et al., 2017). To determine how this grain-averaged abrasion was partitioned along the grain surface, the relative abrasion rate at each point, $v_{\text{abrasion}}(r, \theta)$, was calculated following Equation 1, translated into polar coordinates (r, θ):

$$v_{\text{abrasion}}(r,\theta) = 1 + \int_0^{2\pi} \sqrt{r^2 + \left(\frac{\partial r}{\partial \theta}\right)^2}\, d\theta \cdot \left(r^2 + 2\left(\frac{\partial r}{\partial \theta}\right)^2 - r\frac{\partial^2 r}{\partial \theta^2}\right) \cdot \left(r^2 + \left(\frac{\partial r}{\partial \theta}\right)^2\right)^{-\frac{3}{2}}, \tag{7}$$

where the second term in Equation 7 corresponds to the second term in Equation 1, expressed in polar coordinates, that is,

$$c_1 = \int_0^{2\pi} \sqrt{r^2 + \left(\frac{\partial r}{\partial \theta}\right)^2}\, d\theta, \tag{8}$$

$$\kappa = \left(r^2 + 2\left(\frac{\partial r}{\partial \theta}\right)^2 - r\frac{\partial^2 r}{\partial \theta^2}\right) \cdot \left(r^2 + \left(\frac{\partial r}{\partial \theta}\right)^2\right)^{-3/2}. \tag{9}$$

We assumed that the perimeter of the particle being modeled was representative of the population of particles with which it was interacting. Centered finite differences were used to calculate $\frac{\partial r}{\partial \theta}$ and $\frac{\partial^2 r}{\partial \theta^2}$. Because $v_{\text{abrasion}}(r, \theta)$ is a function of curvature (with the convention that rates ≥ 0 correspond to the

particle surface abrading inward), some points can result in $v_{abrasion}(r, \theta) < 0$, but abrasion cannot cause the particle surface to accrete outward. To resolve this issue, points where $v_{abrasion}(r, \theta) < 0$ were set to $v_{abrasion}(r, \theta) = 0$. Finally, the scaled abrasion rate for each θ, $R_{abrasion}(r, \theta)$, was calculated following Equation 3. The abrasion increment for each θ was obtained by multiplying $R_{abrasion}(r, \theta)$ by a time step duration, dt. For typical sand-size ooids, $dt = 0.0001$ hr was the maximum time step duration that reliably did not introduce singularities into the abraded particle surface. Each abrasion increment was applied by decreasing each $r = f(\theta)$ by the abrasion increment $R_{abrasion}(r, \theta)dt$.

Following each set of simulations for a single pair of cortical layer bounding surfaces, the best fit growth-abrasion history was identified by choosing the set of growth increment and abrasion steps resulting in the minimum value of the sum of squares of misfits between the radius of the simulated bounding surface (r_{model}) and the radius of the bounding surface traced from the thin section (r_{actual}) for the chosen set of 2,000 evenly spaced values of $\theta = (0, 2\pi]$:

$$SS\ misfit = \sum_{\theta=0}^{2\pi} (r_{model}(\theta) - r_{actual}(\theta))^2. \quad (10)$$

The best fit surface was used as the inner bounding surface for simulating the next cortical layer outward from the nucleus; the sequence of growth and abrasion steps described above was repeated for this and all subsequent cortical layers.

After all the cortical layer bounding surfaces in an ooid were simulated, the resulting best fit solutions were evaluated quantitatively using a misfit statistic, defined as the mean of the sum of squares of misfits for each cortical layer, normalized by the cross-sectional area (A) of that cortical layer:

$$misfit\ statistic = \frac{1}{n_{layer}} \sum_{layer=0}^{n_{layer}} \frac{SS\ misfit(layer)}{A(layer)}, \quad (11)$$

where n_{layer} is the number of cortical layers included in the inversion model and $A(layer) = A(r, \theta) = \int_0^{2\pi} \frac{1}{2} r^2 d\theta$. The best fit solutions were also evaluated qualitatively by examining whether or not the model matches gave locally poor fits. The latter criterion was included based on the identification of some cases that yielded a relatively low misfit statistic but contained a locally poor match to the data—this was typically due to the model failing to match the degree of rounding of some angular part of the grain inherited from the nucleus shape. Most of these unsatisfactory fits were associated with ooids with nuclei with irregular shapes that may have included meaningful topology outside of the plane of the thin section and therefore were not captured in the model input data.

Cortical stratigraphic records were compared among ooids by plotting a step function abrasion increments (time) versus growth increments (thickness) using a difference matrix produced by calculating the Fréchet distance between pairs of stratigraphic records. The Fréchet distance is a statistic that compares the similarity of curves that accounts for the order of points in addition to their locations (Fréchet, 1906). This difference matrix was then used to cluster ooid histories via constructing a dendrogram (using the unweighted pair group method with arithmetic means) and nonmetric multidimensional scaling, both as implemented by Matlab 2018b. Metrics of cumulative growth (sum of the best fit growth increments for each cortical layer) and cumulative abrasion (sum of the best fit abrasion durations for each cortical layer) were also used to compare ooid histories.

2.3. Sensitivity Testing

We designed a series of tests to assess the sensitivity of the model to key parameter definitions (H, P, and the parameterization of u_*), subtle differences in user input (i.e., the cortical layer boundary definitions), and the best fit selection. To evaluate the sensitivity of model results to input parameters that affect abrasion rate (H, P), we compared growth-abrasion histories for a representative ooid assuming different values for either H or P, with all other parameters held constant. We also compared growth-abrasion histories using the parameterization of u_* that varies as a function of Rouse number and a constant u_*. To test the sensitivity of the model results to subtle differences in the user input, we traced the cortical layers of a single ooid 10 different times and compared the model histories fit to these (subtly) different inputs. In some cases, an individual

cortical layer was difficult or impossible to trace for its entire circumference; here we sought to assess the potential consequences for omitting such a layer from the model input data. We compared the growth-abrasion histories for a representative ooid made by arbitrarily omitting some or all of the intermediate cortical layers. This test was also used to evaluate how the occurrence of growth-abrasion steps that were not preserved in an ooid cortex—due to subsequent abrasion, for example—might have affected the model results. To assess whether or not the selected best fit growth-abrasion history is representative of the ensemble of good fits (i.e., if it is similar to the next best fits), we evaluated if the 1,000 best fit growth-abrasion histories for a suite of representative ooids converged to similar values.

3. Model Application

3.1. Study Site Background and Sample Collection

Lacustrine ooids from the GSL, UT, were selected for study because their cortical fabrics are commonly very well preserved due to the general absence of microboring Cyanobacteria. Here the ooid nuclei are primarily angular quartz grains or elongated brine shrimp fecal pellets—shapes for which the predicted shape change due to precipitation and abrasion was readily distinguishable because abrasion more readily rounds corners and reduces aspect ratio than does morphometric change associated with precipitation (Figure 2). And the fair weather bed shear velocity in the GSL is typically much lower than that in marine ooid shoals—commonly below the threshold of motion (Eardley, 1938; Halley, 1977; Kahle, 1974; Sandberg, 1975). The latter criterion made these ooids a useful case study to assess whether the effects of abrasion can be recognized in ooids with very infrequent transport and test the assumption that collisional abrasion dominates over frictional abrasion. Six samples of modern ooid sand were collected from the GSL (Figure 3). Four samples (six total subsamples) were collected from Bridger Bay (BB) on Antelope Island: one collected from the shoreline in May 2015—"GSL001" and its subsamples "GSL002," sieved to >500 μm, and "GSL003", sieved to <500 μm (IGSN: IEEJT0001); two collected from the shoreline in September 2017—one, "BB1," from the sediment surface (IGSN: IEEJT001A), and another, "BB4cm," from 4-cm depth, presumably characterized by ooids that had been active less recently (IGSN: IEEJT000Y); and one collected 400-m inland from the shoreline in September 2017, "BB5," presumably characterized by ooids that had been active less recently (IGSN: IEEJT001E). Two samples were collected from near GSL State Park (SP): one collected in September 2017 from the sediment surface, "S7" (IGSN: IEEJT001F), and another in May 2018 from 3 cm below the sediment surface, "SP" (IGSN: IEEJT000R). One sample was collected from near the Spiral Jetty (SJ) in the northern part of the lake in May 2018 (IGSN: IEEJT000K). The sediment surface near the current shoreline in all locations was characterized by small asymmetric and symmetric ripples with ~15 cm wavelengths and some larger bedforms with ~10 cm of relief. All samples were collected during what we interpreted as "fair weather" conditions, during which no ooid transport was observed.

Each sample was rinsed and air dried to remove halite and other evaporative salts from the surfaces and then analyzed for grain size and shape data using a Retsch Camsizer P4 at the University of Colorado Boulder to provide population-level (>250,000 grains) characterization of the sediment population with which to compare individual grain history data. An aliquot of ooids from each sample was affixed in epoxy and prepared as a polished thin section by Spectrum Petrographics (Vancouver, WA). Thin sections were imaged in transmitted and reflected light using a Zeiss AxioImager M2 at the University of Colorado Boulder. Images of exemplar ooids selected from each sample were collected using a 20X objective and z-stacks of at least eight focal distances to improve depth of field. A sample suite of 132 ooids was imaged and traced for model analysis.

3.2. Model Settings

Ooid growth was simulated using a series of fixed surface-normal growth increments following Equation 6 to minimize uncertainty associated with reconstructing Ω, k, and n, all of which depend on lake water chemistry, including salinity and temperature, which varies on seasonal and multiannual cycles. Additional growth was applied at 5 μm increments. Each of the growth simulations was subjected to between 300,000 and 600,000 time steps of duration $dt = 0.0001$ hr. Fluid density was set at $\rho_f = 1.08$ g/cm^3 based on field measurements of the density of GSL water at BB and GSL SP, and fluid kinematic viscosity was set at $\nu_f = 1.3 \times 10^{-6}$ m^2/s following Nayar et al. (2016) and Sharqawy et al. (2010). The lake is presently divided into the less saline South Arm (BB and GSL SP) and the more saline North Arm (SJ), so the lake

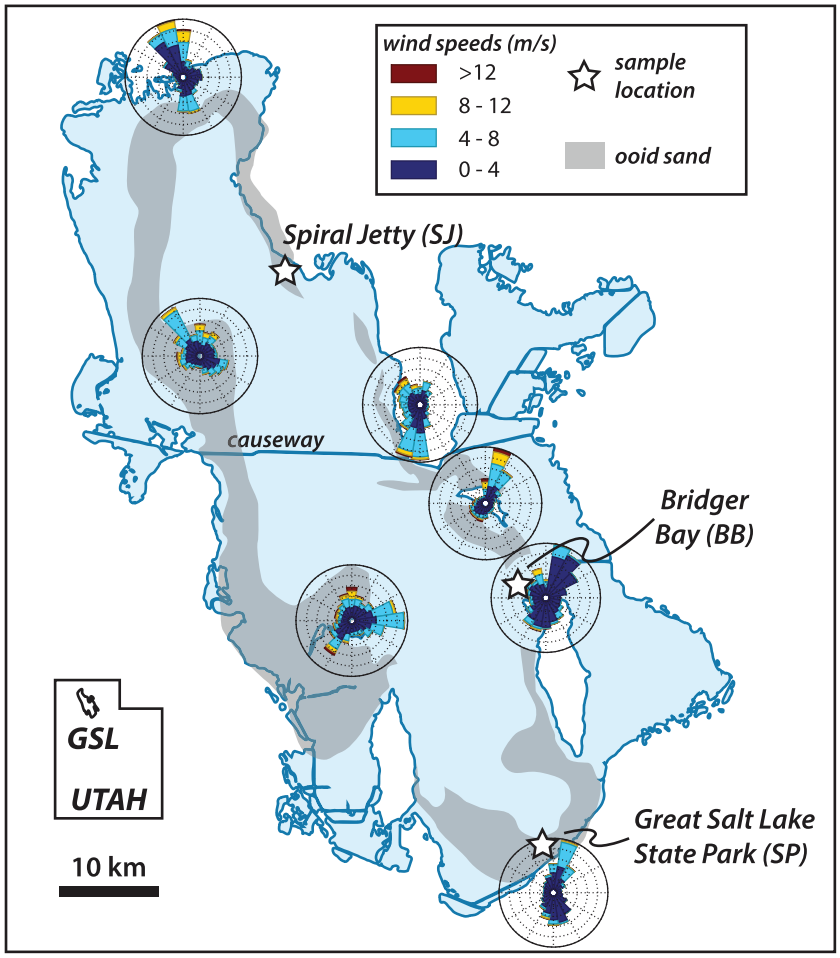

Figure 3. Map of sample locations in Great Salt Lake, UT. Shaded gray areas indicate areas of ooid sand as mapped by Eardley (1938). Rose diagrams show 1 year of wind data from March 2017 to March 2018 from the Mesowest database (Horel et al., 2002) curated by the University of Utah for weather stations adjacent to sample locations and other major ooid sand zones (weather station codes in parentheses): Locomotive Springs (LMS), Gunnison Island (GNI), Promontory Point (PRP), Fremont Island (FREUT), Hat Island (HATUT), Antelope Island (SNX), and Lake Point I-80 (UT9).

water at SJ currently has higher density and viscosity than that at the other two localities. However, considering the contrast between the ~6,000 year lifetimes of GSL ooids from both BB and SJ (Paradis et al., 2017) and the construction of the causeway that caused the North Arm to become more saline in the 1950s, we considered that the density of modern North Arm lake water was not representative of typical conditions for ooid growth at SJ. We assumed a constant $P = 2.5$, consistent with transport at the threshold of suspension; we used Rouse number rather than Yalin number to constrain u_* because it was unclear if current ripples on the exposed sediment surface were representative of transport conditions. We chose water depth $H = 1$ m, noting that abrasion rate is not particularly sensitive to plausible GSL water depths (0.1–2 m) for sand-size grains (Figure S2). The preceding steps resulted in at least 1.5 million total simulations of possible bounding surfaces for each layer.

To evaluate the use of Rouse numbers to estimate u_* (in particular, for applications to the rock record), we used an ArcGIS toolbox designed to calculate wave characteristics and bed shear stress using bathymetry and wind data (Rohweder et al., 2008) to estimate bed shear velocities in GSL; the model applied the procedure of the Shore Protection Manual (U.S. Army Corps of Engineers, 1984) to calculate effective fetch and the algorithms of the Coastal Engineering Manual (U.S. Army Corps of Engineers, 2002) and Shore Protection Manual (U.S. Army Corps of Engineers, 1984) to calculate wave characteristics and bed shear

stress. We used existing GSL bathymetry (Baskin & Allen, 2005; Baskin & Turner, 2006; Tarboton, 2017) and local wind data from the MesoWest database as model inputs; in particular, 1 year of wind data (March 2017 to March 2018) from weather stations UT9 (near GSL SP) and SNX (near BB) were used to assess typical wind conditions. SJ was not directly assessed with this model due to uncertainty associated with restoring bathymetry and fetch to their states preceding the construction of the causeway separating the North and South Arms of the lake in the last century. The wave model therefore provided an assessment of u_* independent of our assumed Rouse number.

Even with initial screening, 31 of the original 132 ooids selected did not produce satisfactory fits and have been omitted from the results presented below. There was a clear cutoff for misfit statistic >2.4 (Figure S3a), while other grains were omitted because of a local poor match for part of the cortex (Figure S3b). Most of these unsatisfactory fits were associated with ooids with nuclei with irregular shapes that may have included topology outside of the plane of the thin section and were therefore not captured in the model input data. If model misfits were related to selection of ooid cross sections that did not include the major axis, the misfit statistic should be inversely correlated with nucleus aspect ratio because nuclei with higher measured aspect ratios are more likely to have captured the major axis (therefore producing better fits and lower misfit statistics); our results did not show this relationship (Figure S3c). If frictional abrasion played a significant role in controlling the evolution of GSL ooid shapes, our model should have repeatedly failed to match the topology of elongated ooids because frictional abrasion during rolling is predicted to focus diminution along the short axis of the grain (Sipos et al., 2018), as opposed to collisional abrasion, which focuses diminution along the long axis. We did not observe such a pattern of mismatches (Figure S3c) and therefore concluded that collisional abrasion was sufficient for characterizing GSL ooids.

4. Results

Grain size analyses revealed broadly similar sediment characteristics among the different samples: median grain sizes (D_{50}) ranged from 231 to 312 μm, mean roundnesses ranged from 0.70 to 0.80, mean sphericities ranged from 0.91 to 0.92, and mean aspect ratios ranged from 1.29 to 1.36 (Table S1). The only notable population-level distinctions between samples were that BB5 (collected ~400 m inland from the active shoreline at the time of collection) was somewhat finer grained than BB samples from the active shoreline (D_{50} = 231 μm vs. 302–312 μm) and that SJ sediment was characterized by a bimodal distribution of grain size. The remaining samples had unimodal grain size distributions (Figure 4).

We considered model results from 101 individual GSL ooids from the three localities (Figure 5): 78 from BB, including 6 different subsamples, as described in section 3.1; 10 of these were from SJ, and 23 from adjacent to GSL SP. The ooids analyzed produced histories with cumulative radial growth of 35–194 μm (mean 105 μm, standard deviation 39 μm, median 104 μm) and cumulative abrasion time of 0–194 hr (mean 61 hr, standard deviation 40 hr, median 58 hr). The largest data set from sample BB4cm spanned nearly this entire range (cumulative growth 44–175 μm and cumulative abrasion time 15–126 hr). Fréchet distances between ooid histories ranged from 4.2 to 220.5 (mean 71.6, standard deviation 35.3). The relatedness of ooid histories as illustrated via both a dendrogram (Figure 6) and an nonmetric multidimensional scaling plot (Figure S4) revealed eight clusters. Comparing growth-abrasion history plots within and among these clusters illustrated trajectories shared within each cluster (Figure 7). Qualitative comparison of images of ooids from each cluster indicated that while some ooids within each cluster appeared similar, the clusters overall did not correspond to identical ooids (Figure 6). As expected, the mean Fréchet distances among ooid histories within each cluster are much lower than those in the full data set—the mean Fréchet distances in seven of the eight clusters are ≤36, about half of the mean Fréchet distance among the whole data set (Table 1). Calculated growth-abrasion histories more clearly differentiated grains among clusters than traditionally measured grain shape metrics like particle aspect ratio defined in successive cortical layer boundaries (Figure S5).

Cumulative abrasion times were not related to nucleus type, diameter, aspect ratio, or external ooid diameter (Figure 8). In general, ooids with more cortical layers identified had a slight tendency to be associated with more cumulative radial growth (R^2 = 0.35) and longer cumulative abrasion time (R^2 = 0.16) (Figure S6). Ooids with more cumulative growth tended to be larger (R^2 = 0.82; Figure S7), but there was no apparent relationship between cumulative growth and nucleus size, aspect ratio, or type (Figures 8 and S7).

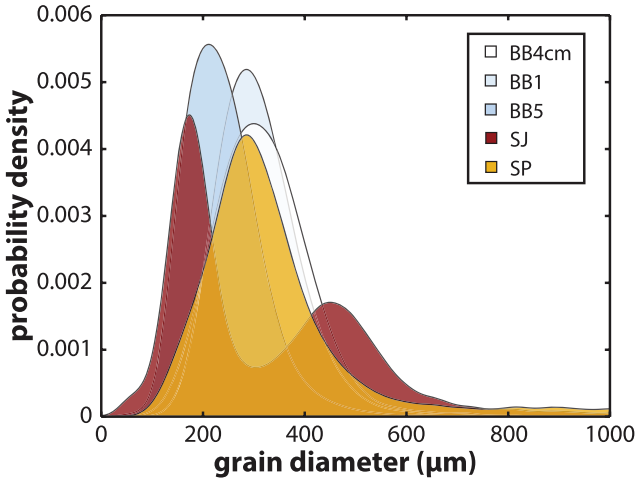

Figure 4. Probability density function estimates for grain diameter distributions of GSL sediment samples included in this study. Note that BB5 (collected ~500 m inland from BB1 and BB4cm, which were both collected at the active shoreline) is somewhat finer than other BB samples and that SJ has a bimodal grain diameter distribution, while all other samples have unimodal grain diameter distributions.

Comparing the cortex thickness (the difference between the nucleus diameter and the external diameter) with the modeled cumulative radial growth for each ooid revealed that all ooids fell at or below a 1:1 line—a feature that implies at least some particle diminution via abrasion (Figure 9). Notably, the slope of these data was lower for BB ooids ($m = 0.81$) than for SJ ooids ($m = 0.92$) or SP ooids ($m = 0.94$). In general, ranges and means of grain characteristics (nucleus diameter and aspect ratio, and external ooid diameter) and model outputs (cumulative growth and cumulative abrasion time) were highly similar among ooids grouped by sample location (Figure 8). SJ appeared to have somewhat lower cumulative abrasion durations than did BB or SP, but this could also reflect the small sample size ($n = 10$) and the underlying bimodal grain size distribution unique to SJ. In contrast, ranges and means of external ooid diameter, cumulative growth, and cumulative abrasion time were distinct among ooids grouped by cluster (Figure 8).

Shear velocities used to calculate abrasion rate ranged from 0.002 to 0.056 m/s—this corresponded with a range in D from the smallest nucleus (56 μm) to the largest ooid (483 μm). Shear velocities estimated using the fetch and wave model varied depending on wind speed and direction. For the representative year, daily mean wind speeds ranged from 0.02 to 12 m/s (mean 2.8 m/s, median 2.5 m/s, standard deviation 1.5 m/s) near GSL SP, with most wind directions from either NNE or south (Figure S9). Near BB, daily mean wind speeds also ranged from 0.02 to 12 m/s (mean 2.9 m/s, median 2.2 m/s, standard deviation 1.9 m/s), with most wind directions from either NNE or SSE (Figure S9). Due to the orientations of shorelines at both BB and GSL SP, winds from the S/SSW produce little fetch, would be expected to produce smaller waves, and therefore minimal values of u_*. Therefore, we focused on modeling waves for wind from 20° (NNE) with either the mean wind speed (2.9 m/s) or the 90th percentile wind speed for that quadrant (5.8 m/s), since the windiest days are all characterized by S/SSW wind directions. The 90th percentile wind speed predicted $u_* = 0.04$–0.06 m/s for BB and $u_* = 0.05$–0.06 m/s for GSL SP, while the mean wind speed predicted $u_* = 0.01$–0.03 m/s for BB and $u_* = 0.02$–0.03 m/s for GSL SP (Figure S10). Therefore, the u_* estimates made via the 90th percentile wind speed overestimated mean u_*, which is better captured by the Rouse number approach (albeit in a

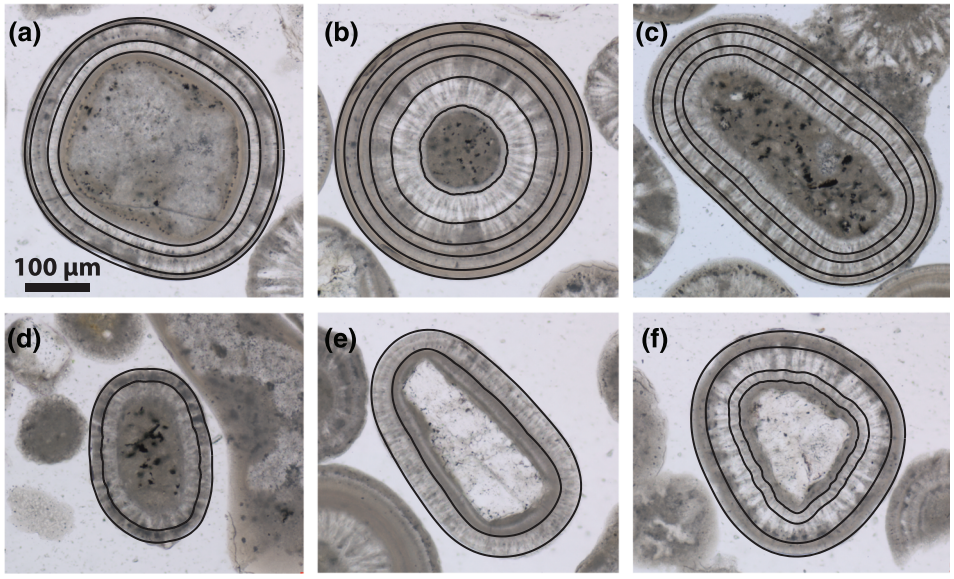

Figure 5. Photomicrographs of exemplar ooids and best fit cortical layer boundaries.

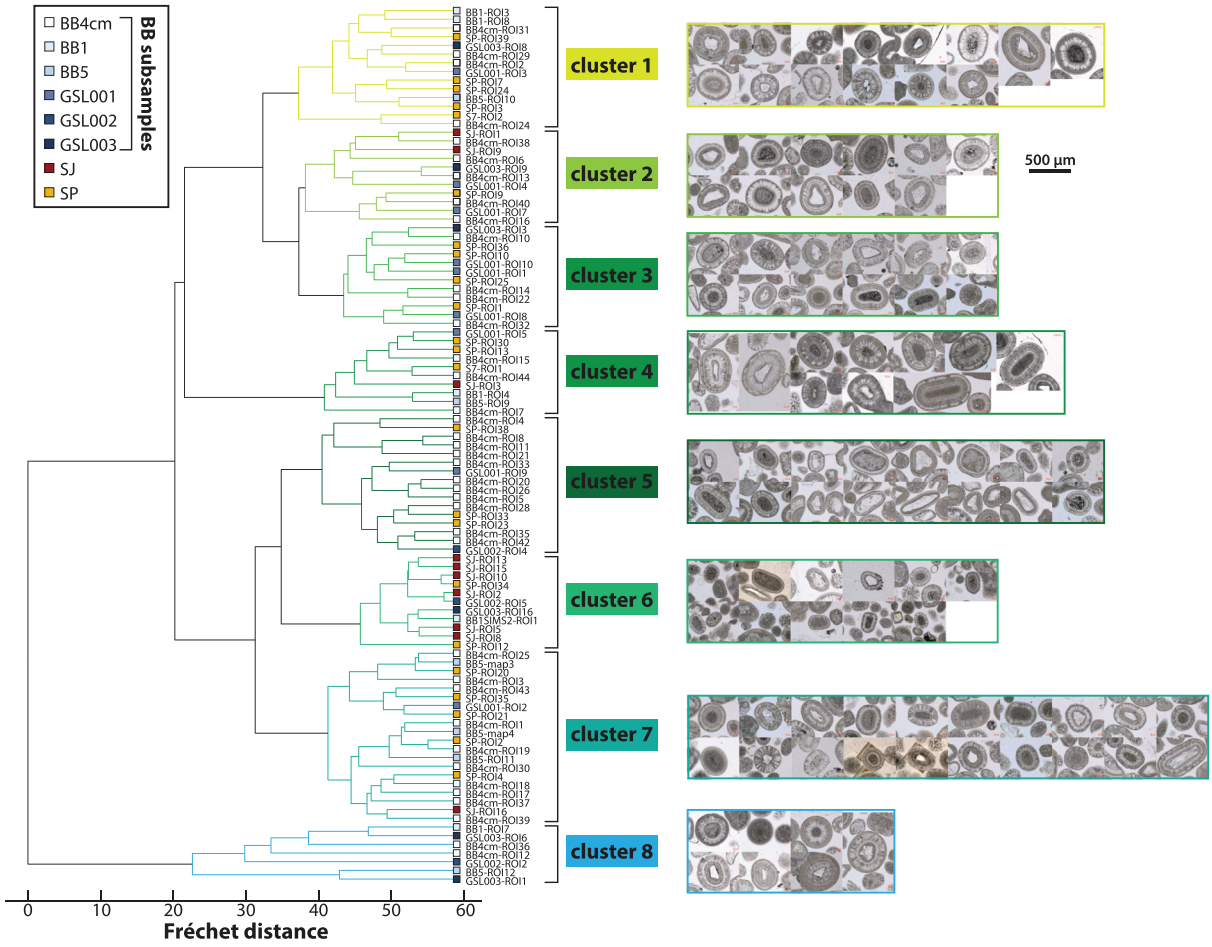

Figure 6. Dendrogram of relatedness between different growth-abrasion histories, as parameterized by Fréchet distance, and thin section photomicrographs of ooids associated with each cluster. Ooids with shorter total horizontal (i.e., parallel to the Fréchet distance axis) path length across the closest shared node more closely related (i.e., shorter Fréchet distance) than those with longer horizontal path length.

manner that ties u_* to D). Furthermore, as a result of the chosen parameterization, the abrasion durations from the model represent abrasion times at or near peak abrasion rate, not necessarily total abrasion time.

The transport parameter sensitivity tests indicated that the growth-abrasion histories were not strongly dependent on water depth or Rouse number estimates. Within the range $H = 0.5–2$ m the growth-abrasion histories were highly similar, while very shallow water depth ($H = 0.1$ m) predicted somewhat less abrasion (Figure 10a); overall, the standard deviations in cumulative growth and abrasion for variable H were small compared to the full data set (2.6 µm growth, 8.1 hr abrasion). Similarly, growth-abrasion trajectories were relatively similar within the range $P = 2–3$ (Figure 10b), with standard deviations that were small for cumulative growth (3.2 µm) and only modestly larger for cumulative abrasion time (11.3 hr). Omitting one cortical layer had only a small effect on the growth-abrasion history, but omitting additional cortical layers resulted in model outputs with substantially less abrasion (Figure 10c), suggesting that the omission of multiple cortical layer boundaries due either to poor preservation or their absence from the preserved cortex due to abrasion would result in the model underpredicting the duration of abrasion. The best fit histories corresponding to the 10 replicate cortical layer traces within a single ooid show that the modeled histories largely converge in terms of cumulative growth and cumulative abrasion (Figures 10d and S11), with standard deviations (8.5 hr abrasion time, 4.4 µm growth) that were much smaller than those of the full 101 ooid data set. There was some variation in histories: 9 of 10 replicates had relatively similar histories, with the 10th as a slight outlier. Fréchet distances ranged from 4.3 to 33.0 (mean 15.9, standard deviation 6.8; Table S2); in other words, the differences between replicates were less than the typical differences between ooids within any of

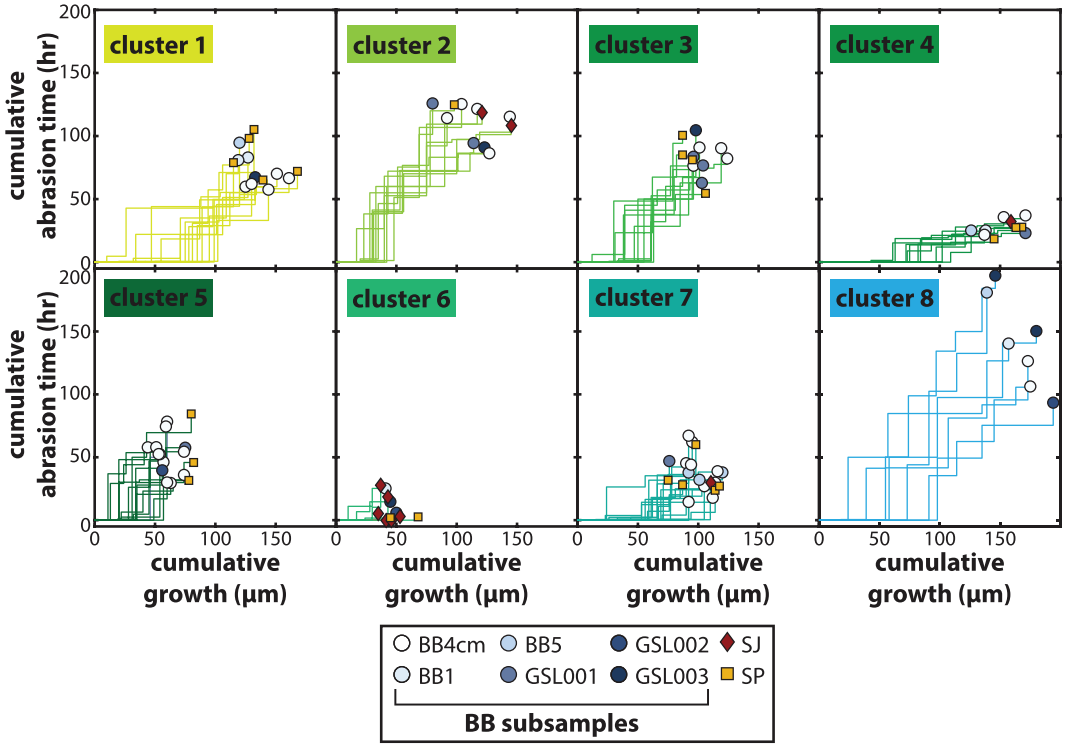

Figure 7. Growth-abrasion histories, with subplots grouped by clusters identified in Figure 5. Growth-abrasion histories in each cluster appear to share similar trajectories. Notably, all clusters except cluster 8 include ooids from at least two localities and four clusters include ooids from all three localities, illustrating that histories are not unique to each locality.

the eight clusters. The best 1,000 histories for an individual grain were nearly identical, demonstrating that the results converged on a good solution (Figure 10e).

Calculating abrasion rate assuming a constant u_* over the lifetime of an ooid rather than a constant Rouse number (such that u_* depends on D) resulted in a different set of predictions for cumulative abrasion (Figure 10f). In a test case, the constant u_* model required substantially more abrasion time to match the innermost cortical layer boundary. This divergence resulted from differences in abrasion rate for these small grain size: At constant u_*, abrasion rate was very low at small D because grains contacted the bed very infrequently ($R_{\text{abrasion, grain avg}} = 0.03$ μm/hr for the innermost cortical layer boundary in the test case); at constant $P = 2.5$, abrasion rate was closer to its maximum value for that particular D at small D because a lower u_* was calculated ($R_{\text{abrasion, grain avg}} = 0.08$ μm/hr). In contrast, the grain-averaged abrasion rates from the two approaches converged for larger grain sizes (for the outermost cortical layer boundary in the test case, $R_{\text{abrasion, grain avg}} = 0.5$ μm/hr for the constant u_* model and $R_{\text{abrasion, grain avg}} = 0.54$ μm/hr for the constant Rouse number model). For ooid populations with a relatively narrow distribution of nuclei sizes, the difference between these two approaches is similar to rescaling the abrasion times for earlier growth-abrasion stages, so histories can still be compared among grains regardless of the approach chosen. Both approaches were simplifications of the transport conditions experienced by any individual ooid over its lifetime. The wind wave u_* estimates indicated that u_* is variable throughout each year, including lower shear velocities at which abrasion rates would be maximized for smaller grains. For this reason, we think the Rouse number u_* estimates better captured the conditions for which abrasion rate were maximized (and thus most likely to outcompete precipitation rate)

Table 1
Summary Statistics of Fréchet Distance Matrices Within Each of Eight Dendrogram Clusters

Cluster	Maximum	Minimum[a]	Mean[a]	Standard deviation[a]
1	54.9	14.7	34.3	9.6
2	67.3	10.5	36.0	11.7
3	50.7	14.0	28.1	7.8
4	46.9	12.7	29.3	9.7
5	58.0	10.0	30.6	10.3
6	39.9	4.2	19.4	7.5
7	53.2	8.6	31.1	9.1
8	111.8	25.0	60.3	22.1

[a]Minimum, mean, and standard deviation exclude the zeros that occur along the diagonal of the difference matrix.

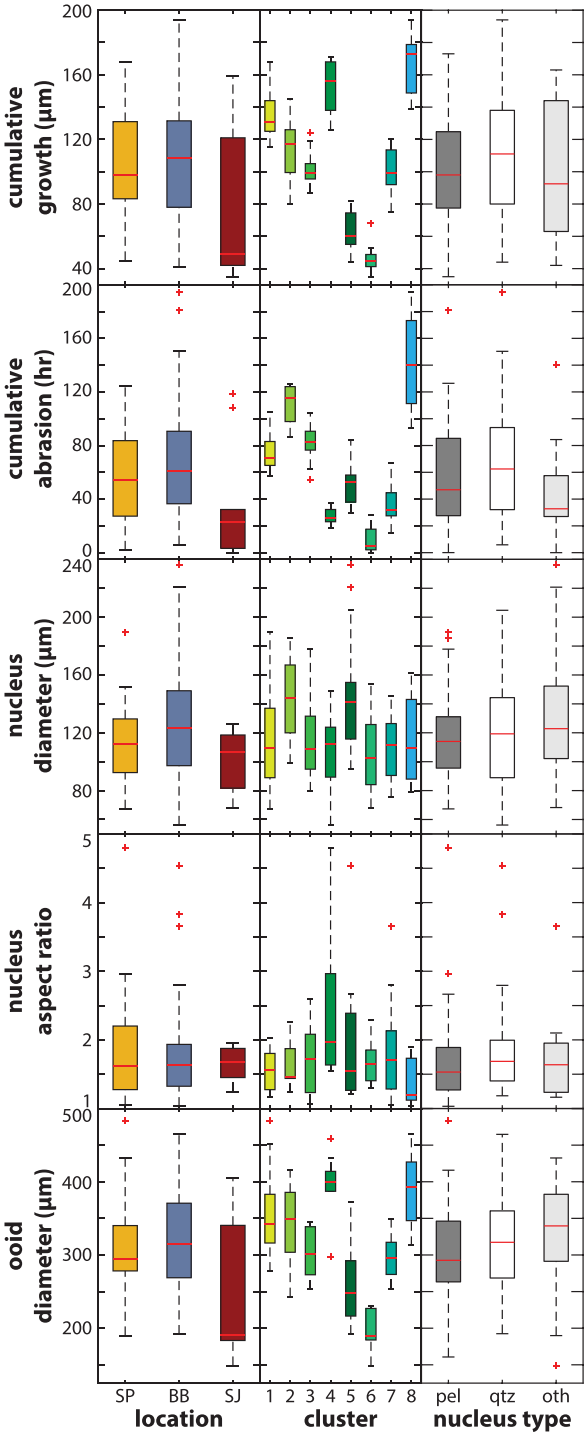

Figure 8. Box plots of model outputs (cumulative growth and cumulative abrasion time) and grain characteristics (nucleus size, nucleus aspect ratio, and ooid diameter), grouped by (left column) location, (middle column) dendrogram cluster, and (right column) nucleus type. Red horizontal lines in each box indicate median value, upper and lower edges of box indicate the 25th and 75th percentiles, the whiskers indicate the upper and lower extreme values, and red "+" symbols indicate outliers. In Figure 8 (middle column), cluster numbers and colors are the same as in Figure 5. In Figure 8 (middle column), "pel" = peloid, "qtz" = quartz, and "oth" = other nucleus composition.

for a particular grain size, rather than assuming a constant u_*. However, this approach using a Rouse number u_* estimate also likely underestimated the total cumulative abrasion time.

5. Discussion

5.1. Comparing Histories of Sediment Grains Among Locations

Do ooids share common histories of growth and abrasion among and/or within each locality? Previous radiocarbon dating of sequential carbonate extractions from ooids has revealed that GSL ooids from both BB and SJ have been accumulating over the past 6,000 years (this time frame reflects the initiation of ooid growth in the environment) (Paradis, 2019; Paradis et al., 2017) and suggests that, on average, ooids in different locations at similar elevations in the lake shared an overall growth duration. Nevertheless, GSL shorelines characterized by ooid sands have a variety of orientations relative to the prevailing wind direction, suggesting that the frequency of transport by wave currents and, consequently, duration of abrasion and its influence on particle growth-abrasion histories might be expected to differ among localities (Figure 3). Comparing characteristics of grain populations among these locations—the traditional toolkit of sedimentological analysis—provided little resolution to determining whether ooid histories differed among locations. The SJ population differed from those of BB and SP in that its grain size distribution is bimodal (Figure 4), but it is not clear why this is the case. Otherwise, the populations of ooids analyzed here were broadly similar in terms of size, shape, and nucleus characteristics (Figures 4 and 8 and Table S1).

But the cortical stratigraphic data presented here provided another approach to comparing sediment among and within these locations. It is striking to find that location (and, putatively, local transport conditions) was not the primary parameter governing ooid histories but instead that all three locations hosted most or all of the types of grain histories identified by our analysis (Figure 6). We identified that the ooids modeled can be grouped into eight clusters representing different types of growth-abrasion histories (Figures 6 and 7), revealing that there are common histories shared not only among grains that are found together (i.e., in the same sample) but more generally among grains from a larger sediment system (i.e., the GSL). These common histories were not related to differences in user input (Figure 10d) or nucleus characteristics (Figure 8). Commonalities among locations suggested that ooid growth has been primarily controlled by regional rather than local factors—that is, that key parameters that controlled ooid growth and abrasion, like $CaCO_3$ saturation state, transport frequency, and bed shear velocity during transport episodes, were not systematically different among different parts of the lakeshore.

The observation of multiple types of histories, however, could reflect different nucleation episodes. For example, the trajectories of ooids in cluster 6 overlap with the initial parts of trajectories in other clusters (Figure 6); the grains in this cluster could therefore reflect relatively young (i.e., more recently nucleated) ooids that could continue to evolve on similar trajectories as some other clusters over time. This interpretation is consistent with the finding that smaller ooids from both Antelope Island and SJ localities tended to have younger bulk radiocarbon ages than did coarser ooids (Paradis, 2019). The bimodal ooid size distribution at SJ could

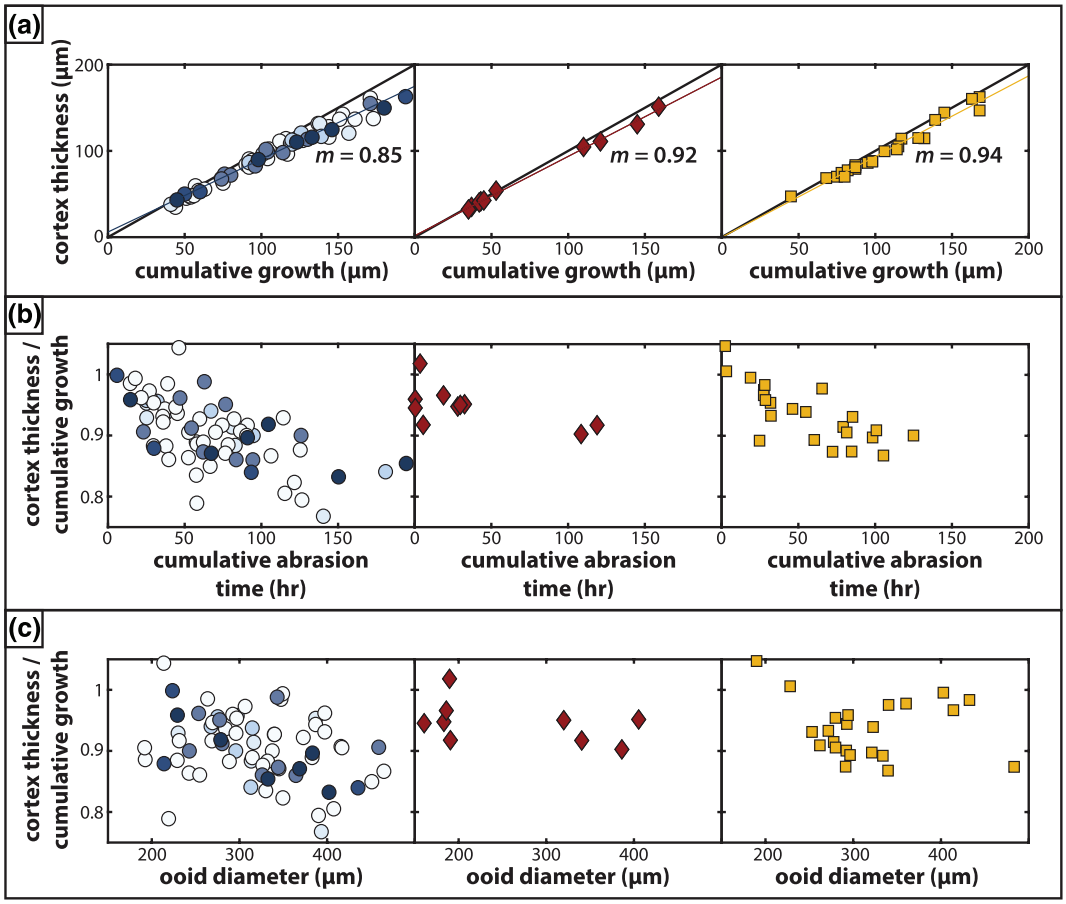

Figure 9. Plots of (a) cortex thickness versus modeled cumulative growth, and the ratio of cortex thickness to cumulative growth versus (b) cumulative abrasion and versus (c) ooid diameter for ooids grouped by sample location: (left column) Bridger Bay (BB), (middle column) Spiral Jetty (SJ), and (right column) Great Salt Lake State Park (SP). Colors and symbols are the same as in Figure 6. (a) Bold black lines indicate a 1:1 relationship, and colored lines indicate linear fits to each sample set. Note that the mean slope (m) for BB is markedly lower than that for SJ or SP, suggesting that more surface-normal growth has been removed by abrasion in BB ooids than in those from SJ or SP (15%, 8%, and 6% removed, respectively). (b) The ratio of cortex thickness to cumulative growth is related to abrasion—the ratio should be ~1 for grains that have experienced no abrasion, and lower values of this ratio indicate more material removed by abrasion. This ratio is inversely correlated with cumulative abrasion time, illustrating that ooids that have been abraded for longer durations have had more material removed. The two axes are different measures of abrasion: Cortex thickness to cumulative growth describes how much material has been removed, while cumulative abrasion time describes a duration of time associated with that material removal. Since grain-averaged abrasion rate (material removed per increment of time) is related to grain size and the grains analyzed have different initial and final sizes, it is not surprising that there is scatter in the data. (c) BB ooids (left column) with larger diameters tend to have lower cortex thickness to cumulative growth ratio, a relationship that is not apparent for other sites. This is consistent with BB ooids experiencing more abrasion later in their growth-abrasion histories—that is, with larger grain diameters and therefore higher grain-averaged abrasion rates (more material removed per unit time). In (b) and (c), four grains have cortex thickness to cumulative growth ratios that are slightly greater than 1, which is an artifact of how these ratios are calculated; in all cases, the measured cortex thickness and modeled cumulative growth differ by ≤3 μm (see data archive at http://doi.org/10.17605/OSF.IO/DSPRH). Figure S8 illustrates the data sets shown in (c), but divided by cluster rather than locality.

therefore reflect a higher proportion of more recently nucleated ooids in the population than that at other localities around the lake. Ooids from multiple BB subsamples were included in all clusters, and in general, the BB subsamples did not correspond to distinct growth-abrasion histories (Figure 6), even though they varied in grain size distribution (Figure 4) and assumed age. The BB growth-abrasion history data therefore suggested that recent historical divergence, marked by the contrast between samples presumably transported less recently (BB4cm and BB5) versus more recently (GSL001, GSL002, GSL003, and BB1), has not been sufficiently long-lasting relative to the overall lifetimes of ooids to produce noticeable differences in grain histories. Historical lake level records indicated that the BB5 locality was fully submerged at the average lake surface elevation over the past 173 years (4,200 ft [1,280 m], 1847 to present) (Emerson & Hooker, 2011; Stephens, 1990); the lake surface elevation was at this historical average level as recently as the late 1980s, suggesting only about ~30 years of divergent histories. The SJ

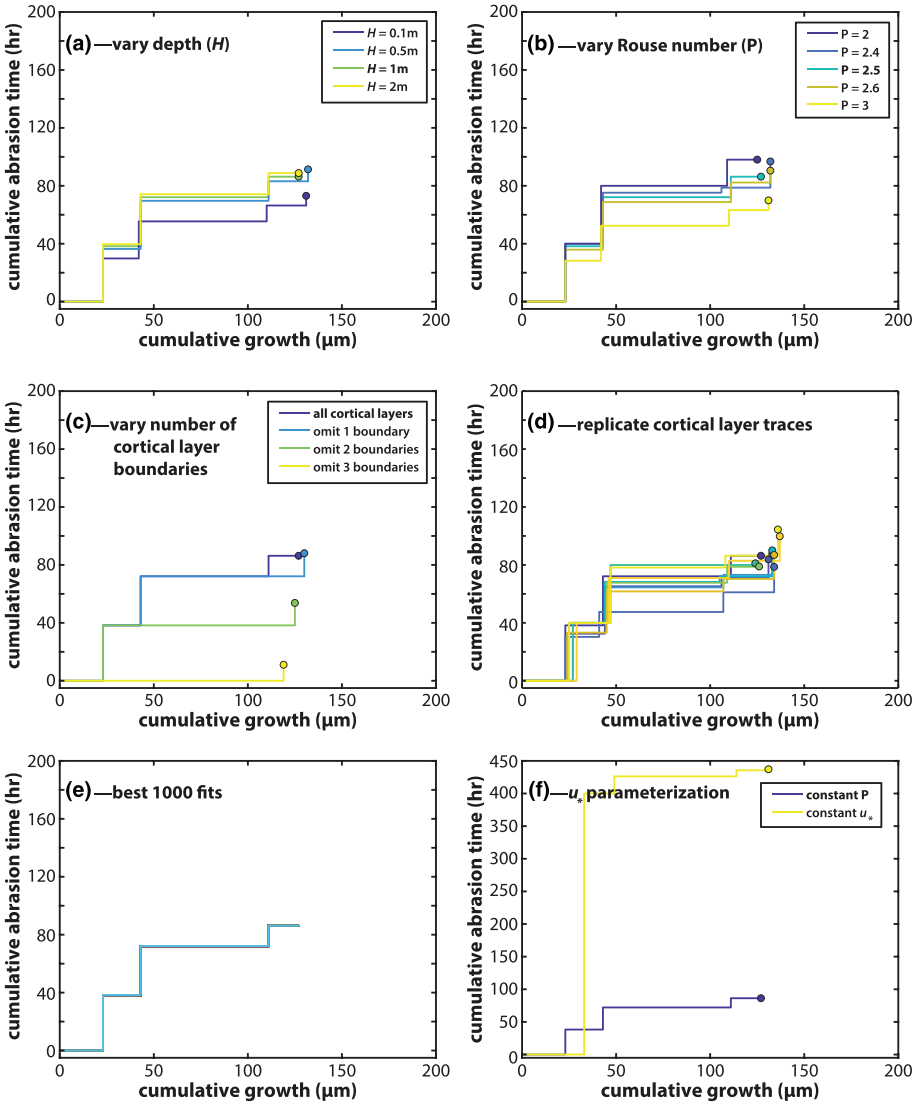

Figure 10. Growth-abrasion history plots showing results of sensitivity tests. Trajectories and (cumulative growth, cumulative abrasion) pairs are similar across a range of (a) water depth and (b) Rouse number. In (c), the trajectory and (cumulative growth, cumulative abrasion) pairs are similar when only 1 cortical layer boundary is omitted but start to diverge substantially, particularly with respect to cumulative abrasion, when additional boundaries are omitted. (d) Although the model outputs of replicate cortical boundary traces were not identical (Figure S11), most replicates had very similar trajectories and (cumulative growth, cumulative abrasion) pairs, illustrating that uncertainty introduced by model inputs was smaller than the typical differences among individual ooids. (e) Best 1,000 growth-abrasion histories for an exemplar ooid; histories are so similar that they overlap when viewed at this scale and line thickness. (f) Comparison of growth-abrasion histories for an exemplar ooid parameterizing u_* via a constant Rouse number versus assuming a constant u_*.

growth-abrasion histories also revealed more information than the population-level data. The SJ sample had a bimodal grain size distribution (Figure 4); the smaller size fraction all fell in cluster 6, interpreted as more recently nucleated ooids, while the larger grains grouped in three different clusters. SJ therefore appeared to have a higher proportion of recently nucleated ooids than did other sites, while the older and larger ooids shared common types of histories with other sites.

One location-specific pattern revealed by the data was the relationship between cortex thickness and modeled cumulative growth. There were, unsurprisingly, linear correlations between these data for all three locations and almost all of the data fell below a 1:1 line (Figure 9a), confirming that some mass loss due to abrasion was necessary to explain the shape evolution of each ooid (Trower et al., 2017). However, the data from BB had a notably lower slope than had those from SJ or GSL SP, indicating that more of the material added through growth had been removed via abrasion. We interpreted this observation to indicate that ooids

in BB have experienced more abrasion more recently in the grains' histories and also when the ooids were larger; under the model parameterization used here, the same increment of time resulted in more material removed from a larger ooid than from a smaller ooid due to the relationship between abrasion rate and grain size. BB ooids with larger diameters also tended to have lower ratios of cortex thickness to cumulative growth (Figure 9c), consistent with them having experienced higher grain-averaged abrasion rates. Unlike the ooid deposits at GSL SP and SJ, which occur on open shorelines facing a basin with substantial fetch, sediment transport in BB has local topographic barriers (the edges of the bay) that limit fetch from some wind directions. In principle, the BB ooid abrasion reconstructions could indicate shifts in prevailing wind direction such that winds producing larger waves and higher bed shear velocities have become more frequent.

5.2. Equilibrium Ooid Size and Ooid Growth Timescales

Trower et al. (2017) demonstrated the concept of an equilibrium ooid size that reflects the balance of precipitation rate and abrasion rate for a given set of conditions (carbonate saturation state, and transport mode and frequency). Are GSL ooids at an equilibrium size? The variability in particle size among the GSL ooid sample sets—and in particular the bimodality of the SJ sample—suggests that the sizes of some of these ooids might not be at equilibrium with respect to current lake conditions. Transport of sand-size sediment in GSL is infrequent, particularly compared with transport frequency in marine ooid shoals ($f = 0.05$–0.25 in modern marine ooid shoals; Bathurst, 1975; Davies et al., 1978; Trower et al., 2018). Assuming that $\Omega_{aragonite} \approx 2$ (measured by Ingalls et al., 2020), the aragonite precipitation kinetics determined experimentally for 35–44 ppt salinities (Zhong & Mucci, 1989) are broadly valid for salinity ≥110 ppt (i.e., salinities of the GSL), and transport at the threshold of suspension ($P = 2.5$), and then equilibrium ooid size (D_{eq}) for the GSL should be between ~271 and ~614 μm, corresponding to transport 5% of the time ($f = 0.05$) or 0.5% of the time ($f = 0.005$), based on the model of Trower et al. (2017) (Figure S12). The median (D_{50}) grain sizes for all localities are within this range (Table S2). These intermittency values are consistent with the 2017–2018 wind data set and the wind wave u_* model: Winds capable of producing bed shear velocity to suspend the larger ooids ($u_* \approx 0.05$ m/s) occurred 1.2% of the time ($f = 0.012$) at GSL SP and 1.8% of the time ($f = 0.018$) at BB. Some ooids within all the GSL populations are therefore within a range of likely equilibrium sizes.

The cumulative growth estimates from the model can also be used to provide a constraint on the duration of net growth. At $\Omega_{aragonite} = 2$ and assuming aragonite precipitation kinetics for seawater salinities (Zhong & Mucci, 1989), a 300 μm diameter ooid should experience ~8 μm/yr radial growth with no abrasion. At this growth rate, the range of cumulative radial growth for modeled ooids (35–194 μm) requires net growth durations of 4.4–25.3 years. Why are these timescales orders of magnitude shorter than the millennial growth lifetimes estimated via sequential radiocarbon dating (Paradis, 2019)? Aragonite precipitation kinetics are not well constrained experimentally for GSL waters, and historical changes in carbonate chemistry in the lake are poorly known. Slower precipitation kinetics translate to longer net growth durations for modeled ooids—but are unlikely to account for the orders of magnitude difference between these rates and the ~6,000 year lifetimes. Ingalls et al. (2020) found that $\Omega_{aragonite} \leq 1$ in shallow GSL porewaters, suggesting that ooid growth is only possible when the grains are at the sediment-water interface or suspended within the water column. Bed shear velocities sufficient to transport GSL ooids are thought to occur infrequently, requiring that GSL ooids spend a substantial proportion of their lifetimes in the shallow subsurface, where they can neither grow nor abrade. Therefore, the difference between the apparent growth durations (4.4–25.3 years) and the ^{14}C-constrained ooid lifetimes (~6,000 years) suggests that ooids were sequestered in the shallow subsurface and neither growing nor abrading for >99% of their lifetime. This finding implies that individual GSL ooid cortices are time averaged in a fashion similar to sedimentary rocks accumulating in sedimentary basins (e.g., Sadler, 1994) and capture only very brief snapshots of lake water and temperature. Furthermore, the brevity of these periods of active time explains why GSL ooids have not achieved equilibrium shapes (Sipos, 2020; Sipos et al., 2018), which would require sufficient time and constant environmental conditions.

The factors affecting precipitation rate (e.g., Ω, temperature, and salinity), transport mode, and transport frequency are all variable over a variety of timescales, from seasonal to decadal, which implies that co-occurring grains are unlikely to have experienced identical combinations of environmental conditions

during all of their infrequent active periods at the sediment-water interface. We therefore interpreted that the variance in grain sizes around D_{eq} reflects the bias inherent to each ooid's brief record (i.e., durations of 4–25 years) of the overall distributions of Ω, temperature, salinity, transport mode, and transport frequency that have occurred in the GSL over the past ~6,000 years. The clusters of ooids identified via our inverse modeling analysis (Figure 6) displayed narrower distributions of grain diameter than did the populations from each locality (Figure 8 and Table S2), indicating that the families of growth-abrasion trajectories shared within each cluster reflect grains that shared similar temporal patterns of activity and therefore equilibrated to similar values of D_{eq}.

6. Conclusions

We developed an approach to reconstruct the growth-abrasion histories of individual ooids via an inverse model of the shapes of cortical layer boundaries, leveraging the unique morphometric rules of surface-normal growth and collisional abrasion. We applied this approach to interpret the cortical stratigraphy preserved within ooids collected from sites around the GSL, UT. Our results demonstrated that there are a set of distinct growth-abrasion histories shared by grains both within populations from a single location and among populations from different locations. We observed subtle differences between ooid populations from each location (evidence of larger recent abrasion rates at BB and a higher proportion of more recently nucleated ooids at SJ), consistent with differences in sediment transport related to local shoreline orientations and transport conditions. Cluster analysis of growth-abrasion histories suggested that the nucleation of ooids in GSL was episodic and that the long durations of inactivity experienced by GSL ooids had more influence on their cortical stratigraphic records than location-specific influences. Our findings demonstrated that carbonate sedimentary grains in a deposit share similar histories, although geochemical analyses that require multiple grains likely still average different histories. The inverse ooid shape modeling approach was capable of identifying coherent histories from ooids in thin section and could be applied to ancient samples to explore environmental variability over timescales shorter than individual ooid lifetimes.

Data Availability Statement

Individual ooid images, cortical layer boundary vectors, best fit model cortical layer boundary vectors, and full Fréchet distance matrix are archived at:http://doi.org/10.17605/OSF.IO/DSPRH. Matlab code designed to aid in identification of cortical layer boundaries from thin section images, run growth-abrasion simulations and identify best fit histories, and plot model outputs (overlays over thin section images, growth-abrasion stair-step plots) are archived at http://doi.org/10.5281/zenodo.3547886.

Acknowledgments

We thank A. Sipos and D. Sumner for constructive reviews that improved the manuscript. E. J. T. acknowledges support from the Agouron Institute Geobiology Postdoctoral Fellowship and NSF EAR Award 1826850. This study was made possible in part due to the data made available by the governmental agencies, commercial firms, and educational institutions participating in MesoWest. W. W. F. acknowledges the support of American Chemical Society Petroleum Research Fund Grant 56757-ND8 and Caltech RI^2.

References

Algeo, T. J., & Watson, B. A. (1995). Calcite, aragonite and bimineralic ooids in Missourian (Upper Pennsylvanian) strata of Kansas: Stratigraphic and geographic patterns of variation. In *Carbonate facies and sequence stratigraphy: Practical applications of carbonate models (a symposium)*, *Society of Economic Paleontologists and Mineralogists Publication* (pp. 95–36). Midland, TX: Society of Economic Paleontologists and Mineralogists.

Baskin, R. L., & Allen, D. V. (2005). *Bathymetric map of the south part of Great Salt Lake, Utah, 2005*. Denver: CO USGS. Retrieved from https://pubs.usgs.gov/sim/2005/2894/

Baskin, R. L., & Turner, J. (2006). *Bathymetric map of the north part of Great Salt Lake, Utah, 2006*. Denver: CO USGS. Retrieved from https://pubs.usgs.gov/sim/2006/2954/

Bathurst, R. G. C. (1975). *Carbonate sediments and their diagenesis*. Amsterdam, The Netherlands: Elsevier.

Bloore, F. J. (1977). The shape of pebbles. *Journal of the International Association for Mathematical Geology*, *9*(2), 113–122. https://doi.org/10.1007/BF02312507

Chow, N., & James, N. P. (1987). Facies-specific, calcitic and bimineralic ooids from Middle and Upper Cambrian platform carbonates, western Newfoundland, Canada. *Journal of Sedimentary Research*, *57*(5), 907–921. https://doi.org/10.1306/212f8ca1-2b24-11d7-8648000102c1865d

Davies, P. J., Bubela, B., & Ferguson, J. (1978). The formation of ooids. *Sedimentology*, *25*(5), 703–730. https://doi.org/10.1111/j.1365-3091.1978.tb00326.x

Dietrich, W. E. (1982). Settling velocity of natural particles. *Water Resources Research*, *18*(6), 1615–1626. https://doi.org/10.1029/WR018i006p01615

Domokos, G., Jerolmack, D. J., Sipos, A. Á., & Török, A. (2014). How river rocks round: Resolving the shape-size paradox. *PLoS ONE*, *9*(2), e88657. https://doi.org/10.1371/journal.pone.0088657

Eardley, A. J. (1938). Sediments of Great Salt Lake, Utah. *AAPG Bulletin*, *22*(10), 1305–1411. https://doi.org/10.1306/3d932ffa-16b1-11d7-8645000102c1865d

Emerson, R., & Hooker, T. (2011). New classification scheme provides an improved tool for managing Great Salt Lake wetlands. *Utah Geological Survey: Survey Notes*, *43*(3), 1–3.

Ferguson, J., Bubela, B., & Davies, P. J. (1978). Synthesis and possible mechanism of formation of radial carbonate ooids. *Chemical Geology*, *22*, 285–308. https://doi.org/10.1016/0009-2541(78)90037-2

Fréchet, M. M. (1906). Sur quelques points du calcul fonctionnel. *Rendiconti Del Circolo Matematico Di Palermo. Second Series*, *22*(1), 1–72. https://doi.org/10.1007/bf03018603

Halley, R. B. (1977). Ooid fabric and fracture in the Great Salt Lake and the geologic record. *Journal of Sedimentary Research*, *47*(3), 1099–1120. https://doi.org/10.1306/212f72ed-2b24-11d7-8648000102c1865d

Heller, P. L., Komar, P. D., & Pevear, D. R. (1980). Transport processes in ooid genesis. *Journal of Sedimentary Research*, *50*(3), 943–951. https://doi.org/10.1306/212f7b2b-2b24-11d7-8648000102c1865d

Horel, J., Splitt, M., Dunn, L., Pechmann, J., White, B., Ciliberti, C., et al. (2002). MESOWEST: Cooperative MESONETS in the western United States. *Bulletin of the American Meteorological Society*, *83*(2), 211–225. https://doi.org/10.1175/1520-0477(2002)083%3C0211:MCMITW%3E2.3.CO;2

Ingalls, M., Frantz, C. M., Snell, K. E., & Trower, E. J. (2020). Carbonate facies-specific stable isotope data record climate, hydrology, and microbial communities in Great Salt Lake, UT. *Geobiology*. https://doi.org/10.1111/gbi.12386

Kahle, C. F. (1974). Ooids from Great Salt Lake, Utah, as an analogue for the genesis and diagenesis of ooids in marine limestones. *Journal of Sedimentary Research*, *44*(1), 30–39. https://doi.org/10.1306/74d7296e-2b21-11d7-8648000102c1865d

Kardar, M., Parisi, G., & Zhang, Y. C. (1986). Dynamic scaling of growing interfaces. *Physical Review Letters*, *56*(9), 889–892. https://doi.org/10.1103/PhysRevLett.56.889

Lamb, M. P., Dietrich, W. E., & Sklar, L. S. (2008). A model for fluvial bedrock incision by impacting suspended and bed load sediment. *Journal of Geophysical Research*, *113*, 225. https://doi.org/10.1029/2007JF000915

Lapotre, M. G. A., Lamb, M. P., & McElroy, B. (2017). What sets the size of current ripples? *Geology*, *45*(3), 243–246. https://doi.org/10.1130/G38598.1

Mariotti, G., Pruss, S. B., Summons, R. E., Newman, S. A., & Bosak, T. (2018). Contribution of benthic processes to the growth of ooids on a low-energy shore in Cat Island, The Bahamas. *Minerals*, *8*(6), 252. https://doi.org/10.3390/min8060252

Maritan, A., Toigo, F., Koplik, J., & Banavar, J. R. (1992). Dynamics of growing interfaces. *Physical Review Letters*, *69*(22), 3193–3195. https://doi.org/10.1103/PhysRevLett.69.3193

Marsili, M., Maritan, A., Toigo, F., & Banavar, J. R. (1996). Stochastic growth equations and reparametrization invariance. *Reviews of Modern Physics*, *68*(4), 963–983. https://doi.org/10.1103/RevModPhys.68.963

Miller, K. L., Szabó, T., Jerolmack, D. J., & Domokos, G. (2014). Quantifying the significance of abrasion and selective transport for downstream fluvial grain size evolution. *Journal of Geophysical Research: Earth Surface*, *119*, 2412–2429. https://doi.org/10.1002/2014JF003156

Nayar, K. G., Sharqawy, M. H., Banchik, L. D., Lienhard, J. H., & V. (2016). Thermophysical properties of seawater: A review and new correlations that include pressure dependence. *Desalination*, *390*, 1–24. https://doi.org/10.1016/j.desal.2016.02.024

Newell, N. D., Purdy, E. G., & Imbrie, J. (1960). Bahamian oölitic sand. *The Journal of Geology*, *68*(5), 481–497. https://doi.org/10.1086/626683

Novák-Szabó, T., Sipos, A. Á., Shaw, S., Bertoni, D., Pozzebon, A., Grottoli, E., et al. (2018). Universal characteristics of particle shape evolution by bed-load chipping. *Science Advances*, *4*(3), eaao4946. https://doi.org/10.1126/sciadv.aao4946

Paradis, O. P. (2019). *Great Salt Lake ooids: Insights into rate of formation, potential as paleoenvironmental archives, and biogenicity (Doctoral dissertation)*. Los Angeles, CA: University of Southern California.

Paradis, O. P., Corsetti, F. A., Bardsley, A., Hammond, D. E., Xu, X., & Walker, J. C. (2017). *Radial ooids from Great Salt Lake (Utah) as paleoenvironmental archives: Insights from radiocarbon chronology and stable isotopes* (Vol. 2017). New Orleans, LA: Paper presented at AGU Fall Meeting Abstracts.

Rohweder, J., Rogala, J. T., Johnson, B. L., Anderson, D., Clark, S., Chamberlin, F., & Runyon, K. (2008). *Application of wind fetch and wave models for habitat rehabilitation and enhancement projects (No. Open-File Report 2008–1200)*. Reston, VA: USGS.

Sadler, P. M. (1994). The expected duration of upward-shallowing peritidal carbonate cycles and their terminal hiatuses. *GSA Bulletin*, *106*(6), 791–802. https://doi.org/10.1130/0016-7606(1994)106%3C0791:TEDOUS%3C2.3.CO;2

Sandberg, P. A. (1975). New interpretations of Great Salt Lake ooids and of ancient non-skeletal carbonate mineralogy. *Sedimentology*, *22*(4), 497–537. https://doi.org/10.1111/j.1365-3091.1975.tb00244.x

Sharqawy, M. H., Lienhard, J. H., & Zubair, S. M. (2010). Thermophysical properties of seawater: A review of existing correlations and data. *Desalination and Water Treatment*, *16*(1–3), 354–380. https://doi.org/10.5004/dwt.2010.1079

Simone, L. (1980). Ooids: A review. *Earth-Science Reviews*, *16*, 319–355. https://doi.org/10.1016/0012-8252(80)90053-7

Sipos, A. A. (2020). Ooid growth: Uniqueness of time-invariant, smooth shapes in 2D. *European Journal of Applied Mathematics*, *31*(1), 172–182. https://doi.org/10.1017/S0956792519000019

Sipos, A. A., Domokos, G., & Jerolmack, D. J. (2018). Shape evolution of ooids: A geometric model. *Scientific Reports*, *8*(1), 1758. https://doi.org/10.1038/s41598-018-19152-0

Steno, N. (1669). *De solido intra solidum naturaliter contento dissertationis prodromus ad serenissimum Ferdinandum II*. Florence: Ex typographia sub signo Stella.

Stephens, D. W. (1990). Changes in lake levels, salinity and the biological community of Great Salt Lake (Utah, USA), 1847–1987. *Hydrobiologia*, *197*(1), 139–146. https://doi.org/10.1007/BF00026946

Sumner, D. Y., & Grotzinger, J. P. (1993). Numerical modeling of ooid size and the problem of Neoproterozoic giant ooids. *Journal of Sedimentary Petrology*, *63*(5), 974–982. https://doi.org/10.1306/d4267c5d-2b26-11d7-8648000102c1865d

Tarboton, D. (2017). *Great Salt Lake bathymetry [data set]*. Hydroshare. Retrieved from http://www.hydroshare.org/resource/89125e9a3af544eab2479b7a974100ba

Trower, E. J., Cantine, M. D., Gomes, M. L., Grotzinger, J. P., Knoll, A. H., Lamb, M. P., et al. (2018). Active ooid growth driven by sediment transport in a high-energy shoal, Little Ambergris Cay, Turks and Caicos Islands. *Journal of Sedimentary Research*, *88*(9), 1132–1151. https://doi.org/10.2110/jsr.2018.59

Trower, E. J., Lamb, M. P., & Fischer, W. W. (2017). Experimental evidence that ooid size reflects a dynamic equilibrium between rapid precipitation and abrasion rates. *Earth and Planetary Science Letters*, *468*, 112–118. https://doi.org/10.1016/j.epsl.2017.04.004

Tucker, M. E. (1984). Calcitic, aragonitic and mixed calcitic-aragonitic ooids from the mid-Proterozoic Belt Supergroup, Montana. *Sedimentology*, *31*(5), 627–644. https://doi.org/10.1111/j.1365-3091.1984.tb01227.x

U.S. Army Corps of Engineers (1984). *Shore protection manual*. Fort Belvoir, VA: Coastal Engineering Research Center.

U.S. Army Corps of Engineers (2002). Coastal engineering manual. *U.S. Army Corps of Engineers, Engineer Manual 1110-2-1100*. Washington, DC: U.S. Army Corps of Engineers.

Zhong, S., & Mucci, A. (1989). Calcite and aragonite precipitation from seawater solutions of various salinities: Precipitation rates and overgrowth compositions. *Chemical Geology*, *78*(3–4), 283–299. https://doi.org/10.1016/0009-2541(89)90064-8